

Computational modeling of MR flow imaging by the lattice Boltzmann method and Bloch equation

Krzysztof Jurczuk^{a,*}, Marek Kretowski^a, Jean-Jacques Bellanger^{b,c}, Pierre-Antoine Eliat^d,
Hervé Saint-Jalmes^{b,c,e}, Johanne Bézy-Wendling^{b,c}

^a Faculty of Computer Science, Bialystok University of Technology, Wiejska 45a, 15-351 Białystok, Poland

^b Signal and Image Processing Laboratory, University of Rennes 1, Rennes, France

^c INSERM U1099, Rennes, France

^d PRISM-Biosit CNRS UMS 3480, INSERM UMS 018-University of Rennes 1-Biogenouest, Rennes, France

^e Centre Eugene Marquis, Rennes, France

ARTICLE INFO

Article history:

Received 30 October 2012

Revised 4 December 2012

Accepted 14 January 2013

Keywords:

Magnetic resonance imaging (MRI)

Fluid flow

Computer modeling and simulation

Bloch equation

Lattice Boltzmann method (LBM)

ABSTRACT

In this work, a computational model of magnetic resonance (MR) flow imaging is proposed. The first model component provides fluid dynamics maps by applying the lattice Boltzmann method. The second one uses the flow maps and couples MR imaging (MRI) modeling with a new magnetization transport algorithm based on the Eulerian coordinate approach. MRI modeling is based on the discrete time solution of the Bloch equation by analytical local magnetization transformations (exponential scaling and rotations).

Model is validated by comparison of experimental and simulated MR images in two three-dimensional geometries (straight and U-bend tubes) with steady flow under comparable conditions. Two-dimensional geometries, presented in literature, were also tested. In both cases, a good agreement is observed. Quantitative analysis shows in detail the model accuracy. Computational time is noticeably lower to prior works.

These results demonstrate that the discrete time solution of Bloch equation coupled with the new magnetization transport algorithm naturally incorporates flow influence in MRI modeling. As a result, in the proposed model, no additional mechanism (unlike in prior works) is needed to consider flow artifacts, which implies its easy extensibility. In combination with its low computational complexity and efficient implementation, the model could have a potential application in study of flow disturbances (in MRI) in various conditions and in different geometries.

© 2013 Elsevier Inc. All rights reserved.

1. Introduction

Magnetic resonance (MR) images of vascular structures play a very important role in clinical angiography [1]. Many diseases are directly related to changes in vessel structures, and a lot of these modifications can appear in medical images. Signal intensity enhancements may indicate hypervascularized areas of tumoral lesions (e.g., hepatocellular carcinoma) [2]. In contrast, flow-related signal voids can appear in the place of serious vessel shape perturbations (e.g., aneurysm, stenosis) [3,4]. Hence, the ability to understand MR flow images and to predict consequences of changes in vascular geometries is crucial.

Although MR imaging (MRI) is known as a highly detailed three-dimensional (3D) imaging modality, there are still a lot of difficulties in vascular image interpretation. This is mainly due to flow-induced disturbances appearing in such areas, caused by intravoxel phase

dispersion (IVPD) [5], misregistration [6,7] or inflow/outflow effects [8]. Moreover, imperfections and limitations of hardware continue to reduce the effectiveness and accuracy of fluid motion characterization and visualization. This motivates the creation of computational models of MR flow imaging as a tool to enhance understanding of involved processes. For instance, they can help to study the relationship between vascular geometry changes and hemodynamic factors in silico [9]. The connection between fluid flow and image appearance can also be investigated [4]. Turning on/off particular physical phenomena and evaluation of various combinations of MRI equipment parameters are often time consuming or even impossible. On the other hand, in computational models, it is far easier to switch on/off their components and to study contribution of each factor alone or together. Therefore, such modeling can certainly contribute to increase our understanding of pathological processes and to improve MRI sequence design. Finally, controlled simulation experiments are also a valuable way of education [10].

There were many studies on flow influence on MRI, both experimental and by simulations, e.g., [4–9,11–20]. Most of them are focused on a chosen imaging sequence/technique and chosen

* Corresponding author. Tel.: +48 85 746 91 07; fax: +48 85 746 90 57.

E-mail addresses: kjurczuk@pb.edu.pl, krzysztof.jurczuk@univ-rennes1.fr (K. Jurczuk).

geometry and flow pattern, e.g., on balanced steady-state free precession (b-SSFP) in simple geometry [8], spiral imaging [7], phase contrast imaging in a carotid bifurcation [19] or slice selection process [11,17]. In contrast to them, in this paper, we propose a more general approach in computational modeling of MR flow imaging with a computer program allowing fast simulations of the effect of complex flow geometries in arbitrary imaging procedure. Our goal is not to concentrate on one particular geometry but to provide extensible solution that integrates geometry, flow and MRI managing modules to increase understanding and unravel their interactions by efficient tests of many scenarios (parameters).

The proposed computational model consists of two connected components: a fluid dynamics component and an MRI one. The first one is responsible for flow modeling by the lattice Boltzmann method (LBM) [21] in given geometries. It provides flow maps which are then used in the second component of the model. This second component reproduces the MRI process. During the imaging simulation, a newly proposed magnetization transport algorithm is used to model the flow influence. The algorithm is based on the Eulerian coordinates approach (i.e., stationary frame [22]). MRI processes are modeled with the use of the discrete time solution of the Bloch equation [23] by means of local magnetization rotations and exponential scaling [24]. These analytical magnetization transformations closely follow the physical process of MRI and in combination with the magnetization transport algorithm naturally incorporate flow-related artifacts. As a result, no additional mechanism is needed to consider the flow influence during most MRI processes (including excitation, relaxation, precession as well as space encoding and signal sampling in 3D objects), in contrast to the one of the most advanced prior works [4,19]. This also implies that the whole imaging procedure for various sequences (e.g., spoiled gradient echo or b-SSFP) with different view ordering (e.g., linear, centric or cyclic) or with different k -space trajectory (e.g., radial or spiral) is straightforward to model, unlike in previous studies [7,8]. Another advantage of the proposed solution is its implementation (computer program) that allows to easily control modeling parameters starting from geometry specification, through flow and MRI, and ending on image processing. These features render the solution as a tool that is user friendly and manageable at different levels, which facilitates running series of simulations with different physiological and imaging parameters. In this study, as a first step, we focus on magnitude images acquired in the spoiled gradient echo sequence. Our initial efforts to create the presented solution are described in the conference paper [25].

In the second section of the paper, the proposed computational model and its implementation (integrated simulation environment) are described. Simulation and experimental setups, used in model validation, are also presented. In the Results section, the validation of the model is performed by comparison between experimental and simulated images as well as by quantitative analysis. The computational performance is also investigated. Finally, in the Discussion section, the model is confronted with prior works, its limitations and advantages are described, and also future works are sketched.

2. Methods

At the beginning, the two parts of the model are described. Then, the way of flow influence incorporation in MRI modeling is presented. Next, the integrated simulation environment (computer program implementing the model with additional supporting modules) is briefly described. Finally, the simulation and experiment setups, used to validate the model, are presented.

2.1. Fluid flow modeling

In the proposed solution, LBM [21] is applied to model fluid flow. This method has been intensely developed over the last two decades,

becoming a powerful alternative to the numerical solving of Navier–Stokes equations known as the conventional computational fluid dynamics mechanism [26]. Many theoretical analysis [27] and numerical investigations [28,29] have shown that LBM is commonly recognized as a method able to simulate realistic fluid flows obeying the Navier–Stokes equations with high accuracy.

LBM is a mesoscopic method placed in between microscopic molecular dynamics and continuous macroscopic approaches [30]. It does not consider each elementary particle alone but treats the behavior of a collection of particles as a unit whose properties are represented by a particles distribution function. Therefore, LBM preserves most of the advantages of both micro- and macroscopic approaches. Its clear physical insight into molecular processes provides easy treatment of boundary conditions and, consequently, high applicability for complex geometries [31]. At the same time, the relevant quantities (e.g., mass, energy, etc.) are conserved at the macrocontinuous regime, like in the Navier–Stokes equations. Moreover, it shows numerous computational advantages, e.g., good stability properties or simple arithmetic calculations. Finally, owing to the intrinsic space–time locality of LBM (i.e., in each time step, only data from neighboring lattice nodes are needed), it is ideal for parallel computing [32].

In LBM, fluids consist of a set of discrete nodes creating regular lattices. At each lattice node, the virtual particles (represented by their distribution function) reside. At discrete time moments, these particles can move along specified directions to the neighboring nodes (propagation step). When the particles meet, they collide (collision step), but they always stay on the lattice nodes. The collision rules are set according to the conservation laws of mass (i.e., number of particles), momentum and energy. The exact conservation laws are fulfilled, not only their numerical approximations. These two steps are expressed by a mathematical formula known as the lattice Boltzmann equation:

$$f_i(\mathbf{r} + \mathbf{e}_i \Delta t, t + \Delta t) - f_i(\mathbf{r}, t) = \Omega_i(\mathbf{r}, t), \quad (1)$$

where $f_i(\mathbf{r}, t)$ is the particle distribution function in the grid node located at position \mathbf{r} at the time t and streaming in the next time step Δt in the direction i with the velocity \mathbf{e}_i . Ω is the collision operator standing for collision rules of the simulated physical phenomenon.

Using the Bhatnager–Gross–Krook (BGK) model [33], the collision operator (complex integro-differential expression) is simplified by the widely used, single-time relaxation approximation [31]:

$$\Omega_i(\mathbf{r}, t) = 1/\tau (f_i^{\text{eq}}(\mathbf{r}, t) - f_i(\mathbf{r}, t)), \quad (2)$$

where τ is the dimensionless relaxation time related to fluid viscosity. The local equilibrium distribution function f_i^{eq} is given by [34]:

$$f_i^{\text{eq}} = \rho \omega_i \left[1 + \frac{3}{c^2} \mathbf{e}_i \cdot \mathbf{u} + \frac{9}{2c^4} (\mathbf{e}_i \cdot \mathbf{u})^2 - \frac{3}{2c^2} \mathbf{u} \cdot \mathbf{u} \right], \quad (3)$$

where $\mathbf{u} = \frac{1}{\rho} \sum_{i=0}^{n-1} \mathbf{e}_i f_i$ is the macroscopic lattice velocity, $\rho = \sum_{i=0}^{n-1} f_i$ is the dimensionless lattice density, ω_i is the weighting factor of a lattice topology and c is the lattice constant related to a propagation factor on the lattice and is set to unity in most cases [34]. Lattice velocity is a fraction of distance between neighboring nodes traveled by fluid per time step (e.g., lattice velocity of 0.5 means that the fluid moves 0.5 lattice cell in time step Δt). To obtain the physical macroscopic velocity, the lattice velocity is multiplied by $\Delta d/\Delta t$, where Δd is the lattice cell size (distance between neighboring lattice nodes).

In two-dimensional (2D) fluid flows, we use the model with $n = 9$ discrete velocities (D2Q9) (Fig. 1A) where

$$\begin{aligned} e_0 &= [0, 0]c & \omega_0 &= 4/9 \\ e_{1,2}, e_{3,4} &= [\pm 1, 0]c, [0, \pm 1]c & \omega_{1,4} &= 1/9 \\ e_{5,\dots,8} &= [\pm 1, \pm 1]c & \omega_{5,8} &= 1/36 \end{aligned}$$

while in 3D ones, the model with $n = 19$ discrete velocities (D3Q19) (Fig. 1B) is selected:

$$\begin{aligned} e_0 &= [0, 0, 0]c & \omega_0 &= 1/3 \\ e_{1,2}, e_{3,4}, e_{5,6} &= [\pm 1, 0, 0]c, [0, \pm 1, 0]c, [0, 0, \pm 1]c & \omega_{1..6} &= 1/18 \\ e_{7,...,10}, e_{11,...,14}, e_{15,...,18} &= [\pm 1, \pm 1, 0]c, [\pm 1, 0, \pm 1]c, [0, \pm 1, \pm 1]c & \omega_{7..18} &= 1/36. \end{aligned}$$

In the presented solution, fluid is considered as a Newtonian incompressible liquid [35]. At entrances and exits of the geometry, it is possible to enforce the constant velocity or pressure boundary conditions. The unknown values of the distribution function are calculated by the extrapolation method proposed by Guo et al. [36]. With respect to the walls, the procedure called the bounce-back scheme (i.e., no-slip) is applied [31]. It rotates the distribution function values on walls so that they return to the fluid in the next time step. We also adopted the modification of f_i^{eq} function (splitting the density into constant contribution and small deviations) proposed by He et al. [27] to increase the accuracy in modeling of incompressible fluids.

2.2. Modeling of MRI

The 3D imaged area (object) is divided into small cubic elements to which basic magnetic resonance parameters (i.e., proton density, relaxation times) are assigned. Every such element can be interpreted as a collection of magnetic spins.

The behavior of spins in the cubic elements in time t during MRI is modeled by the Bloch equation [23]:

$$\begin{aligned} \frac{d\mathbf{M}(\mathbf{r}, t)}{dt} &= \gamma(\mathbf{M}(\mathbf{r}, t) \times \mathbf{B}(\mathbf{r}, t)) \\ &\quad - \frac{M_x(\mathbf{r}, t)\hat{\mathbf{i}} + M_y(\mathbf{r}, t)\hat{\mathbf{j}}}{T_2(\mathbf{r})} - \frac{M_z(\mathbf{r}, t) - M_0(\mathbf{r})\hat{\mathbf{k}}}{T_1(\mathbf{r})}, \end{aligned} \quad (4)$$

where $\mathbf{M} = M_x\hat{\mathbf{i}} + M_y\hat{\mathbf{j}} + M_z\hat{\mathbf{k}}$ is the spin's magnetization vector, \mathbf{B} represents the applied magnetic field, M_0 is the equilibrium magnetization determined by the proton density, T_1 and T_2 are the relaxation times, γ is the gyromagnetic ratio (42.6 MHz/T for hydrogen nuclei), $\mathbf{r} = x\hat{\mathbf{i}} + y\hat{\mathbf{j}} + z\hat{\mathbf{k}}$ is the spatial coordinate vector of a cubic element (set of spins) and $\hat{\mathbf{i}}, \hat{\mathbf{j}}, \hat{\mathbf{k}}$ are the unit vectors in the x, y, z directions, respectively. The applied magnetic field \mathbf{B} is specified as follows:

$$\mathbf{B}(\mathbf{r}, t) = B_1^{\text{RE}}(\mathbf{r}, t)\hat{\mathbf{i}} + B_1^{\text{IM}}(\mathbf{r}, t)\hat{\mathbf{j}} + [B_0 + \Delta B(\mathbf{r}) + \mathbf{r} \cdot \mathbf{G}(t)]\hat{\mathbf{k}}, \quad (5)$$

where $B_1 = B_1^{\text{RE}} + B_1^{\text{IM}}$ is the complex radiofrequency (RF) pulse in the rotating frame, B_0 is the main static magnetic field, ΔB represents the local magnetic field inhomogeneities and \mathbf{G} is the applied magnetic field gradients at position \mathbf{r} .

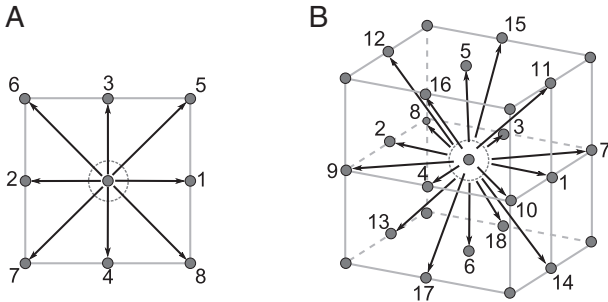


Fig. 1. Lattice topology for (A) D2Q9 model and (B) D3Q19 one. The neighboring nodes are labeled according to numbers of discrete velocities \mathbf{e}_i . Particles move in all these directions during the propagation step based on the values of the particle distribution function. The circle in D2Q9 model and the sphere in D3Q19 one denote that the velocity vector equals zero, i.e., for nonmoving particles.

In the presented model, the discrete time solution of the Bloch equation proposed by Bittoun et al. [24] was applied. It uses the rotation matrices and exponential scaling to represent magnetic events in MRI sequences. Such an approach (used in many advanced MRI simulators, e.g., SIMRI [37], ODIN [38]) allows us to follow the variations of spins' magnetization during the whole MRI sequence without any integration. In each cubic element, the following mathematical formulas are used to calculate the spins' magnetization after successive time steps Δt :

$$\mathbf{M}(\mathbf{r}, t + \Delta t) = \mathbf{A}_{\text{MRI}}(\mathbf{r}, \Delta t)\mathbf{M}(\mathbf{r}, t), \quad (6)$$

$$\mathbf{A}_{\text{MRI}} = \mathbf{E}_{\text{RELAX}}\mathbf{R}_z(\theta_G)\mathbf{R}_z(\theta_{\text{IH}})\mathbf{R}_{\text{RF}}, \quad (7)$$

where \mathbf{A}_{MRI} represents the MR influence modeled as follows:

$\mathbf{E}_{\text{RELAX}}$ is responsible for the relaxation phenomena:

$$\mathbf{E}_{\text{RELAX}}(\mathbf{r}, \Delta t) = \text{diag}[\exp(-\Delta t/T_2(\mathbf{r})), \exp(-\Delta t/T_2(\mathbf{r})), 1 - \exp(-\Delta t/T_1(\mathbf{r}))], \quad (8)$$

\mathbf{R}_z is the rotation matrix about the z -axis used to model the effect of the spatial encoding gradients \mathbf{G} (rotation through θ_G angle) and magnetic field inhomogeneities ΔB (rotation through θ_{IH} angle):

$$\mathbf{R}_z(\theta) = \begin{bmatrix} \cos\theta & \sin\theta & 0 \\ -\sin\theta & \cos\theta & 0 \\ 0 & 0 & 1 \end{bmatrix}, \quad (9)$$

$$\theta_G(\mathbf{r}, \Delta t) = \mathbf{G} \cdot \mathbf{r} \gamma \Delta t, \quad (10)$$

$$\theta_{\text{IH}}(\mathbf{r}, \Delta t) = \gamma \Delta B(\mathbf{r}) \Delta t, \quad (11)$$

while \mathbf{R}_{RF} is the rotation matrix describing the influence of RF pulse and a slice selection gradient (more details in Bittoun et al. [24]).

Based on Faraday's law of an electromagnetic induction [39] and on the assumption that two orthogonal perfect detecting coils lie along the x - and y -axes, the MR complex signal coming from the imaged object at time t is modeled as:

$$\mathbf{S}(t) = \sum_{\mathbf{r}_O \in C} M_x(\mathbf{r}_O, t)\hat{\mathbf{i}} + \sum_{\mathbf{r}_O \in C} M_y(\mathbf{r}_O, t)\hat{\mathbf{j}}, \quad (12)$$

where C is the collection of all cubic elements in the virtual object. Signal values calculated (sampled) during the acquisition period are arranged in the readout k -space matrix. Within a single repetition period, the detected signal fills one k -space matrix row. Each subsequent excitation is performed with a different phase encoding step, and the acquired signals fill the successive matrix rows.

The MR image is created by applying the fast Fourier transform (FFT) [40] to the stored signal. The size of the image voxel is determined by the magnetic field gradient settings. In other words, the number of frequency/phase encoding steps determines the number of voxels in the gradient direction and, consequently, the number of cubic elements assigned to each voxel.

2.3. Combined modeling of MRI and fluid flow

In the center of each cubic element, one LBM grid node is placed. This kind of discretization associates each cubic element (part of tissue) with the MR characteristics (proton density and relaxation times) as well as with the hydrodynamic properties, i.e., mean velocity and direction of the fluid filling it (represented by the dimensionless lattice velocity $\mathbf{u} = u_x\hat{\mathbf{i}} + u_y\hat{\mathbf{j}} + u_z\hat{\mathbf{k}}$ coming from the flow model). The flow velocity for stationary tissue structures (e.g., vessel walls, bones, parenchyma) equals zero.

The process of MR flow imaging is divided into sufficiently small time steps. The longest time step ought to be shorter than the shortest

time needed by the fluid to go from one grid node to another one, which is equivalent to the Courant–Friedrichs–Lewy condition [41] with the Courant number equals 1. After each time step Δt , the local magnetizations of all cubic elements are evaluated, taking into account both the flow influence and the MR phenomena (excitation, relaxation, etc.). This iterative process is modeled by the following equation:

$$\mathbf{M}(\mathbf{r}, t + \Delta t) = \mathbf{A}_{\text{MRI}}(\mathbf{r}, \Delta t) [\mathbf{M}(\mathbf{r}, t) + \Delta \mathbf{M}_{\text{FLOW}}(\mathbf{r}, \Delta t)], \quad (13)$$

where $\Delta \mathbf{M}_{\text{FLOW}}$ and \mathbf{A}_{MRI} represent the flow and the magnetic resonance influences, respectively, during the time period Δt on the magnetization $\mathbf{M}(\mathbf{r}, t)$ of the cubic element placed at position \mathbf{r} .

Fig. 2 presents the general scheme of the coupled algorithms. First, the flow influence is computed by transport of magnetization fractions between neighboring grid nodes. By the use of velocity values and the flow direction, the fractions of magnetization leaving cubic elements (black rectangles labeled by "A," "B" and "C") are propagated to the neighboring nodes. It means that values of magnetization fractions leaving as well as entering for each cubic element have to be evaluated. These operations allow us to model the influence of flowing magnetic spins on the magnetization volume distribution. Next, the MR influence is calculated according to Eq. (6) (Fig. 2, MRI processes). Afterwards, the algorithm returns to the first (flow) step.

The mean magnetization changes caused by flow in a cubic element at position \mathbf{r} during a time step Δt are expressed as follows:

$$\Delta \mathbf{M}_{\text{FLOW}}(\mathbf{r}, \Delta t) = \Delta \mathbf{M}_{\text{IN}}(\mathbf{r}, \Delta t) - \Delta \mathbf{M}_{\text{OUT}}(\mathbf{r}, \Delta t), \quad (14)$$

where $\Delta \mathbf{M}_{\text{IN}}$ denotes the inflow magnetization, while $\Delta \mathbf{M}_{\text{OUT}}$ is the outflow magnetization. For description clarity, the equations of $\Delta \mathbf{M}_{\text{IN}}$ and $\Delta \mathbf{M}_{\text{OUT}}$ are presented in the full form only for the 2D case. The $\Delta \mathbf{M}_{\text{OUT}}$ value is calculated based on the flow properties and the local magnetization of the considered cubic element:

$$\Delta \mathbf{M}_{\text{OUT}}(\mathbf{r}, \Delta t) = \mathbf{M}(\mathbf{r}, t) [|u_x(\mathbf{r})| (1 - |u_y(\mathbf{r})|) + |u_x(\mathbf{r})| |u_y(\mathbf{r})| + (1 - |u_x(\mathbf{r})|) |u_y(\mathbf{r})|]. \quad (15)$$

The graphical interpretation of this equation is presented in Fig. 2. The black rectangles ("A," "B" and "C") represent the magnetization fractions (successive components of the sum in Eq. (15)) leaving the considered cubic element. Meanwhile, the inflow magnetization value $\Delta \mathbf{M}_{\text{IN}}$ is calculated with the use of the magnetizations of neighboring elements and flow properties of the considered cubic element as follows:

$$\begin{aligned} \Delta \mathbf{M}_{\text{IN}}(\mathbf{r}, \Delta t) = & \mathbf{M}\left(\mathbf{r} - \Delta d \frac{u_x(\mathbf{r})}{|u_x(\mathbf{r})|} \hat{\mathbf{i}}, t\right) |u_x(\mathbf{r})| (1 - |u_y(\mathbf{r})|) + \\ & \mathbf{M}\left(\mathbf{r} - \Delta d \frac{u_x(\mathbf{r})}{|u_x(\mathbf{r})|} \hat{\mathbf{i}} - \Delta d \frac{u_y(\mathbf{r})}{|u_y(\mathbf{r})|} \hat{\mathbf{j}}, t\right) |u_x(\mathbf{r})| |u_y(\mathbf{r})| + \\ & \mathbf{M}\left(\mathbf{r} - \Delta d \frac{u_y(\mathbf{r})}{|u_y(\mathbf{r})|} \hat{\mathbf{j}}, t\right) (1 - |u_x(\mathbf{r})|) |u_y(\mathbf{r})| \end{aligned} \quad (16)$$

For 3D objects, the Eqs. (15) and (16) have six cases, i.e., with $|u_z(\mathbf{r})|$ and $(1 - |u_z(\mathbf{r})|)$ additional components for each 2D case.

2.4. Integrated simulation environment

The proposed combined algorithms are extended to a complete modeling environment composed of several modules (Fig. 3) and next implemented as a computer program. The object generation module enables us to specify the regions occupied by different kinds of tissue (Fig. 3, point 1). Special attention is paid to fluids. It is possible to define the geometry of vascular trees composed of cylindrical or cone-

shaped vessels. Moreover, distortions to vascularized geometries can be introduced by adding or removing spaces bounded by geometrical figures (e.g., cylinders, spheres) (Fig. 3, point 2).

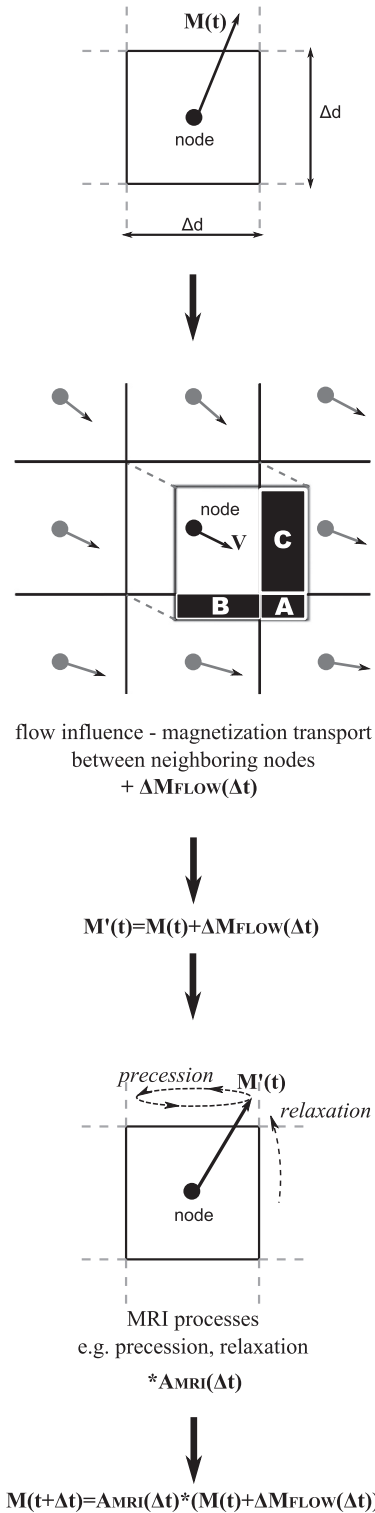


Fig. 2. Coupling of magnetization transport and MRI algorithms. The magnetization at time t is represented by $\mathbf{M}(t)$. In order to calculate the magnetization after a Δt time step, firstly, the flow modifications are taken into account. As a result of magnetization exchange between neighboring nodes ($\Delta \mathbf{M}_{\text{FLOW}}(\mathbf{r}, \Delta t)$), the magnetization changes to $\mathbf{M}'(t)$. Secondly, the MRI processes are considered, and the sought magnetization $\mathbf{M}(t + \Delta t)$ is found. The black filled rectangles labeled by "A," "B" and "C" represent the magnetization fractions that flow out from the node.

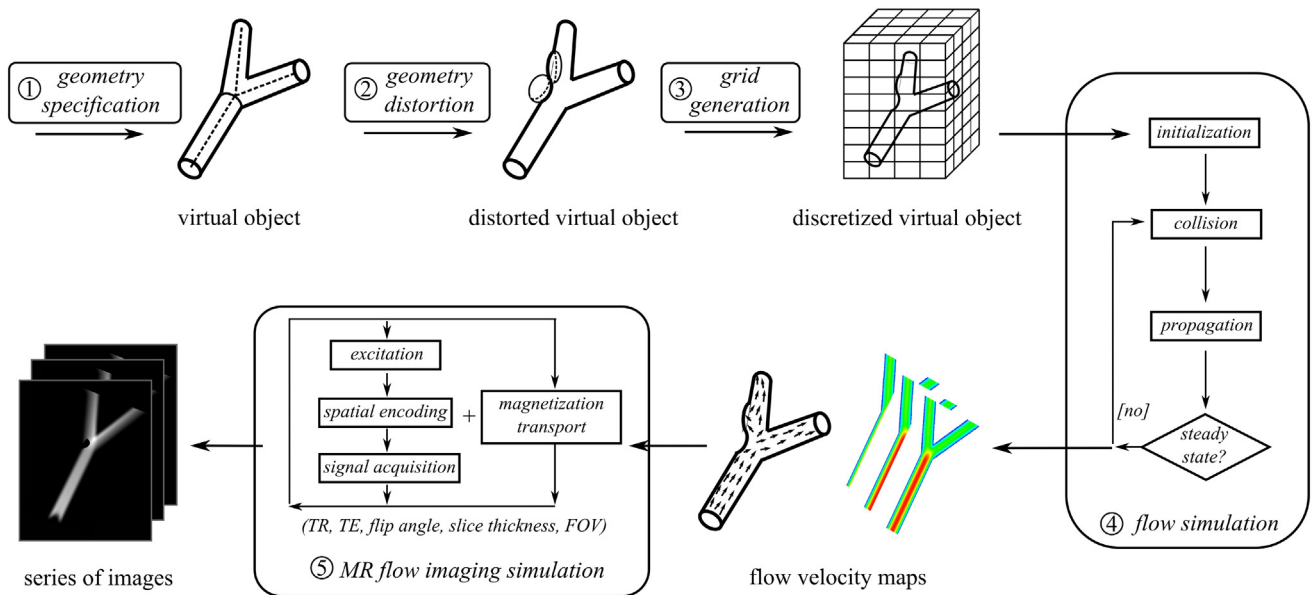


Fig. 3. The modeling environment of MR flow imaging. It consists of several modules which make it possible to control a broad range of parameters. The first module is used to define the basic specifications for virtual objects (e.g., structure of vascular trees). Shape distortions can be introduced in the second module. In order to adapt object data to the LBM and MRI algorithms, the third module performs the data discretization, while the fourth one performs flow simulations. As a result, flow maps are produced which are then used in the simulations of MR flow imaging. Finally, series of MR images are obtained.

In the next step, the object is divided into cubic elements with fixed volume (Fig. 3, point 3). Each cubic element inherits characteristics of the tissue which fills it most. A Gaussian noise can be added to imitate the natural variability of tissue properties. In the case of liquids, borders (e.g., walls and input/output) are found and marked. The flow simulation module produces the velocity maps by performing alternatively the collision and propagation steps (Fig. 3, point 4) until the desired convergence criterion is satisfied, which is until the global absolute difference of the velocity fields (with L2 norm) between successive iterations is smaller than $10e-6$.

The final stage is the MRI modeling (Fig. 3, point 5). Currently, there is a possibility to simulate spoiled gradient echo and spin echo sequences. They can be extended by adding flow compensation mechanisms, such as gradient moment nulling of the desired order for slice selection and readout gradients. Various RF pulses can be chosen, instantaneous (ideal and without any fluid motion influence) or finite duration ones of different shapes (sinc-shaped, rect-shaped or Gauss-shaped) [42]. A Gaussian noise can be also added to the k -space matrix values to imitate thermal noise that usually corrupts the MRI signal [43].

The fluid motion influence can be easily turned off to provide the possibility to study the flow influence on the different MRI steps selectively. Moreover, in order to speed up calculations, the simulation time step may be different during the various stages of imaging, e.g., shorter during a slice selection and longer after a signal acquisition until a next excitation.

The simulation environment is implemented in C++ programming language and hence can be compiled to be run under Windows, Linux and Mac operating systems. Parameters of all modules can be specified by input files. Moreover, basic graphical user interface, which is still under development, allows to control MRI simulations and to visualize the virtual object and the simulated images. A flow visualization package enables one to observe how flow maps evolve starting from the LBM algorithm initialization until the stability condition is reached.

2.5. Simulation and experiment setups

All MRI experiments were conducted on a Bruker Biospec 4.7-T scanner (Bruker Biospin, Wissembourg, France) by the spoiled

gradient echo sequence (FLASH), with and without flow compensation along the slice-selective and frequency-encoding directions. Two physical glass phantoms were used. The first phantom was a rigid, straight tube with radius of 3 mm (Fig. 4A), while the second one was a rigid, U-bend shape tube with radius of 4 mm (Fig. 4B). Flow of (cold tap) water was considered. Flow rates were measured with a graduated cylinder and a stopwatch. The water source was placed several meters from the MRI scanner. In order to obtain fully developed steady flows, long straight entrances before MRI measurement location were provided (about 2 m).

In all simulations, the spoiled gradient echo sequence was used. Fluid behavior was modeled as a steady flow of a Newtonian liquid with literature-based properties for 10 °C pure water: kinematic viscosity of $1.3 \times 10^{-6} \text{ m}^2 \text{ s}^{-1}$, T_1 of 2500 ms, T_2 of 2500 ms [13,44]. Constant pressure boundary conditions at inlets/outlets were applied. Five cubic elements per direction were arranged to each voxel based on previous studies [14,18,38] and our own investigation to search good-compromised values in the context of image quality, simulation time and LBM resolution. A personal computer equipped with Intel Core i7 CPU (1.73 GHz) and 8 GB of RAM was used. We verified the solution under Linux with GCC version 4.3.2 compiler and also under MS Windows 7 in MS Visual Studio 2005.

In the case of the straight tube geometry, the mean velocity was set to 0.4 ms^{-1} (Reynolds number = 900). The imaging parameters were as follows: repetition time (TR) = 200 ms, echo time (TE) = 5 ms, flip angle (FA) = 30°, in-plane resolution $0.47 \text{ mm} \times 0.47 \text{ mm}$ with slice thickness of 1 mm, field of view = $60 \times 60 \text{ mm}$, sinc-shaped RF pulse. Images in axial and sagittal planes were acquired as well as with and without flow compensation gradient of first order along slice-selection and frequency-encoding directions.

In the case of the U-bend geometry, the mean velocity was set to 0.38 ms^{-1} (Reynolds number = 1150). The imaging parameters were as follows: TR = 50 ms, TE = 5/10/20 ms, FA = 40°, in-plane resolution $0.5 \text{ mm} \times 0.5 \text{ mm}$ with slice thickness of 3 mm, field of view = $64 \text{ mm} \times 64 \text{ mm}$, sinc-shaped RF pulse.

Flow and fluid parameters (i.e., mean velocity, viscosity, Reynolds number, etc.) and detailed imaging settings were equal in both experiments and the corresponding simulations. Based on the

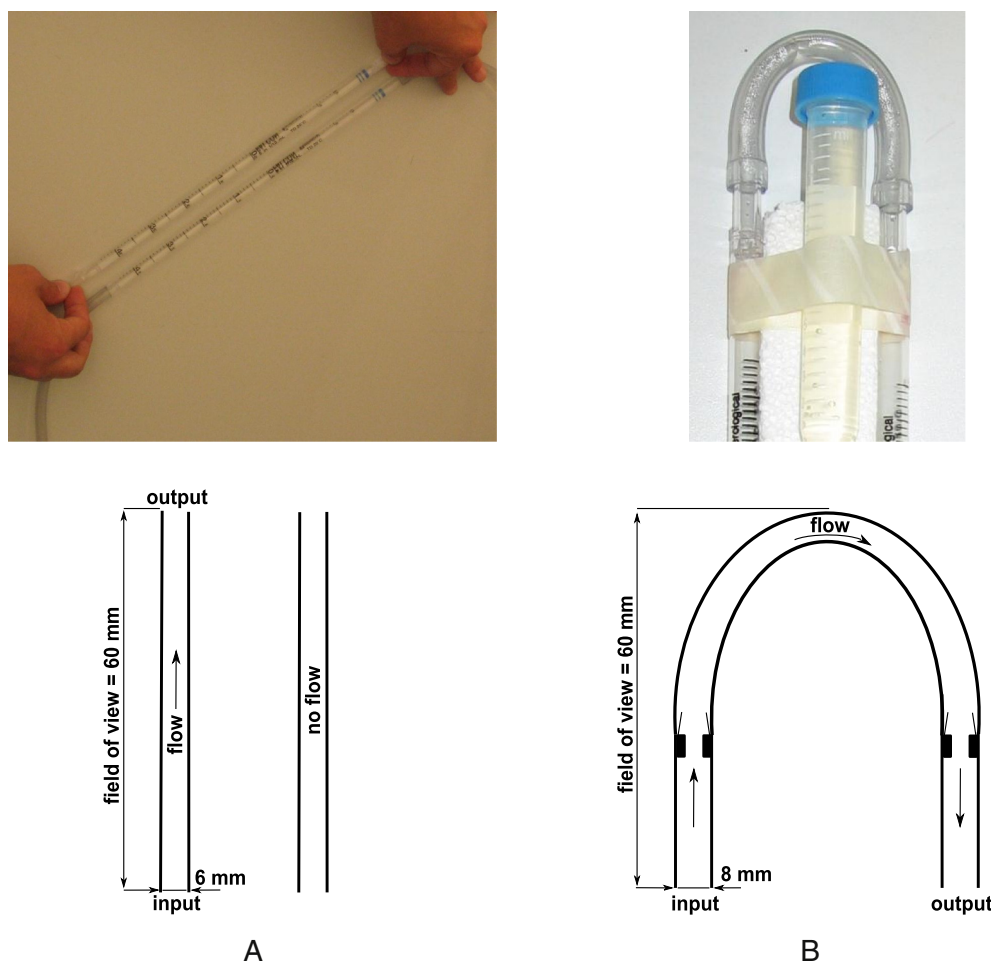


Fig. 4. Geometry of the phantoms used in MR flow imaging experiments: (A) straight rigid tube, (B) U-bend rigid tube. Second-row images present sketches of 2D projections of the phantoms.

Reynolds number, long entrance length and series of test measurements, we identified that flow in experiments had a parabolic profile.

In simulated images of the 2D flow geometries that are commonly studied in other computational solutions of MR flow imaging, the flow and MR measurement conditions were set in accordance to previous papers [18,19]. For the straight tube lying diagonally to the gradient axes, laminar flow with mean velocity equals 0.35 ms^{-1} was forced, while imaging parameters were $TR = 400 \text{ ms}$, $TE = 25 \text{ ms}$, $FA = 30^\circ$, in-plane resolution $2 \text{ mm} \times 2 \text{ mm}$, field of view $= 200 \times 200 \text{ mm}$. For the single stenosed carotid bifurcation, steady flow with maximum velocity of 4.7 ms^{-1} in the stenosis was considered. Imaging parameters were $TR/TE = 50/5$, $200/5$ and $50/15 \text{ ms}$, $FA = 30^\circ$, in-plane resolution $0.25 \text{ mm} \times 0.25 \text{ mm}$, field of view $= 20 \text{ mm} \times 65 \text{ mm}$.

3. Results

In this section, the proposed solution is experimentally verified. First, the computational model is validated by comparison between experimented and simulated images as well as by quantitative analysis. Finally, the computational performance is investigated.

3.1. Model validation

Fig. 5 presents the comparison of simulated and experimental MR images in a straight tube phantom (Fig. 4A) with laminar flow. Under the images, corresponding normalized signal intensity profiles through

their centers horizontally are also provided. The first-row images were acquired in the sagittal plane. In the images obtained without any flow compensation mechanism (Fig. 5A, B), the IVPD artifact is clearly visible. It results in a partial signal cancellation away from the tube center. A wide distribution of velocities (particularly large within voxels close to walls) across the tube with laminar flow produces significant phase variations within the voxels and can lead to a high signal decrease. When the flow compensation mechanism was incorporated (first-order gradient moment nulling), the IVPD artifact was greatly reduced (Fig. 5C, D). This mechanism ensured phase coherence at the center of the echo, regardless of flow velocity.

The second-row images in Fig. 5 were obtained in the axial plane. The IVPD artifact is again clearly visible at regions close to the tube walls where the high range of velocities within voxels causes a signal diminution (Fig. 5A, B). Similarly, images acquired with the first-order compensated sequence show a significant reduction in signal loss. A good agreement between simulated and experimental images (as well as between signal intensity profiles) is observed.

We investigated in detail the flow influence on the RF excitation step. The MRI simulations of the straight tube phantom in an axial plane (second row in Fig. 5) were considered. Fig. 6 presents curves of transverse magnetization phase for cubic elements just after the slice selection step, both along (Fig. 6A) and across the tube (Fig. 6B). The curves in Fig. 6C and D show magnetization phase from simulations with no flow. A coherence of cubic element phases inside the chosen slice in both directions is easily observable. Phase curves coming from simulations with flow (without any flow

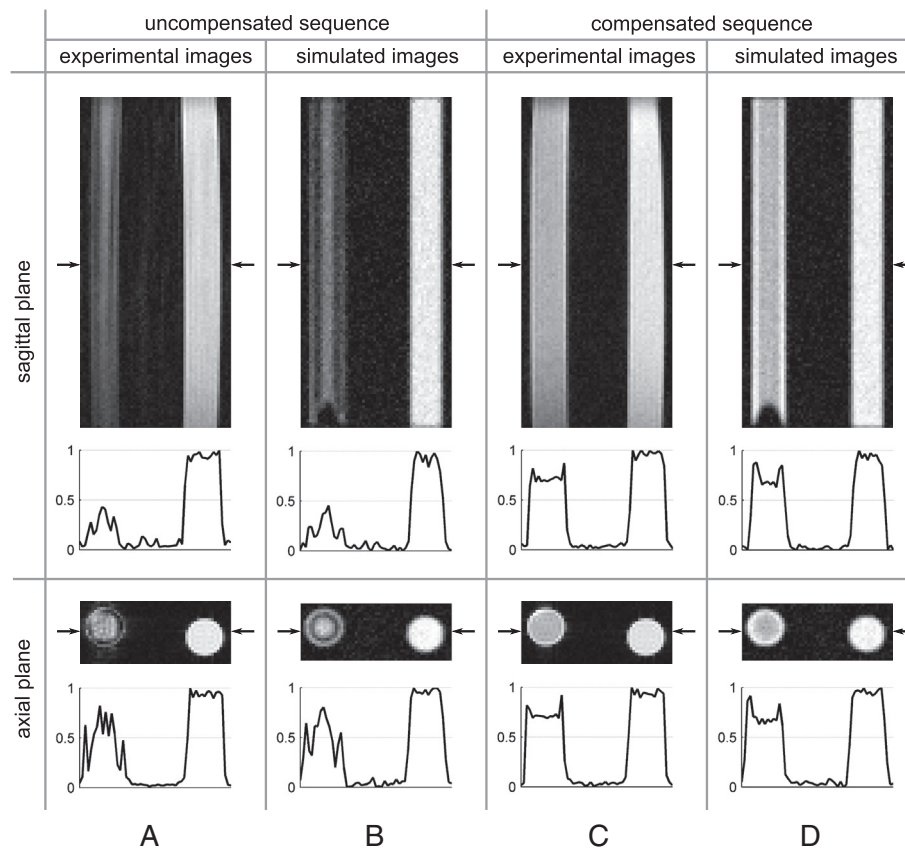


Fig. 5. MR images (simulated and experimental) and corresponding normalized signal intensity profiles through their centers horizontally (arrows) of a 3D straight tube phantom. First row images were acquired in sagittal plane, while the second row images in axial plane. The images in columns (C) and (D) were acquired with the flow compensation mechanism: velocity compensation gradient of first order along slice-selection and frequency-encoding directions. Frequency encoding in the vertical direction and phase encoding in the horizontal one. Significant black background in images around tubes was dropped.

compensation mechanism) are presented in Fig. 6E and F. These curves show that cubic elements along the main flow direction are totally dephased, even in the excited slice. Also, across the tube, phase values in neighboring cubic elements can differ significantly. Moreover, the phase dispersion in regions close to walls is much higher than that in the center of the tube (as a result of higher range of velocities; Fig. 6F). This dephasing is at the origin of what can be observed in the second-row images in Fig. 5A and B: IVPD artifact takes place and signal loss appears just in the voxels close to walls, where strong phase gradients exist.

When the flow compensation gradient is applied, the phase dispersion along the tube inside the excited slice (Fig. 6G) is much smaller than without compensation (Fig. 6E). Moreover, a high coherence of phase is observed across the tube (Fig. 6H). In the second-row images in Fig. 5C and D, we can easily observe that this flow compensation mechanism is able to eliminate or at least effectively minimize flow-related artifacts.

The MR images of the U-bend phantom (Fig. 4B) are presented in Fig. 7. Here, our attention is focused on the displacement (misregistration) artifact [6] since it dominates the results. This artifact usually appears due to fluid motions obliquely to gradient axes. Then, unavoidable time delays between subsequent spatial encoding steps cause various coordinates to be encoded at different times and consequently reconstructed at displaced positions. In our case, the misregistration arises mainly from the time interval between phase and frequency encodings. As a result, the horizontal and vertical positions are encoded at different times. In both experimental and simulated images (Fig. 7), a distortion of the tube lumen in the phase-encoding direction is easily visible. It can be

also observed that the displacement increases with the TE augmentation since the time interval between phase and frequency encoding enlarges when TE grows.

The displacement also depends on the flow velocity. Thus, in the case of the parabolic laminar fluid flow, the central part of the flow is the most shifted. The combined influence of flow velocity and TE on the displacement can cause the faster part of flow to be reconstructed on top of adjacent slower parts. This overlapping can result in signal enhancement which is observed along the outer wall of the left part bend and inner wall of the right part bend when TE equals 5 and 10 ms. When TE reaches 20 ms, a band of signal even appears outside the tube lumen. Moreover, the wide range of velocities of parabolic flow causes a significant distribution of displacement, leading to an important dispersion of the signal intensity and finally to the disappearance of the tube lumen. To present the difference in displacement artifact in other flow patterns, images of plug flow (uniform velocity) were simulated (bottom-row images in Fig. 7). The equal velocity across the tube provides a uniform displacement giving no distortion of the tube lumen. The areas of low and high image intensities seen in the simulated results qualitatively correlate with the corresponding regions of experimental images.

Fig. 8 presents simulated MR images of the 2D geometries that commonly appear in other works. In the case of the straight tube lying diagonally to the gradient axes [6,18], the simulated MR image is dominated by the displacement artifact. Because of the parabolic flow pattern, different parts of the tube are displaced at different distances, which leads to the signal enhancement along one wall and signal diminution across the tube. As regards the carotid bifurcation geometry [4,12,16,19], the simulated MR images reveal more

complicated flow artifacts: signal enhancement along the divider wall of the bifurcation because of misregistration and low intensity in the stenosis where strong velocity gradients cause dephasing. Different combinations of parameters show that shortening TR increases signal loss due to the saturation effect, while the increase of TE causes strong signal loss in voxels with a wide range of velocities. Results are in a good agreement with the other computational models cited before.

3.2. Performance evaluation

Table 1 presents mean time measures of MRI simulations performed to obtain the presented images. For 2D objects (no slice selection, all cubic elements were excited), the computation time is noticeably lower (e.g., in comparison to the Marshall model [18]), even for bigger objects of size 640×1280 cubic elements. When 3D objects were tested, the computation time naturally increases. However, it is still relatively short for these kinds of simulations, e.g., in comparison to the Marshall solution [19]. Besides the object dimension and object/image size, other factors influence the simulation time and can be adjusted to perform quick test imaging,

e.g., time step during the various stages of imaging or repetition time. Direct comparison with other solutions of MRI flow modeling is difficult because, in most of the studies, exact time measurements were not provided.

4. Discussion and conclusions

The presented comparison of simulated and experimental images proves that the proposed approach is able to model MR flow imaging. Although not all image features are in an excellent agreement, most of them are reproduced successfully. In the case of the straight tube phantom, subtle differences can be noted close to the tube walls. Moreover, the simulated uncompensated sequence produces a slightly more signal loss than in experiments where the ring of voxels with IVPD artifact is thinner. These differences can be caused by the incompletely modeled imaging process, e.g., ideal spoiling of transverse magnetization compared to spatially nonuniform spoiling in reality or approximated rectangular gradient waveforms in simulations.

It can be also observed that in simulated images (Fig. 5B, D; sagittal plane), a prominent parabolic signal void appears at the

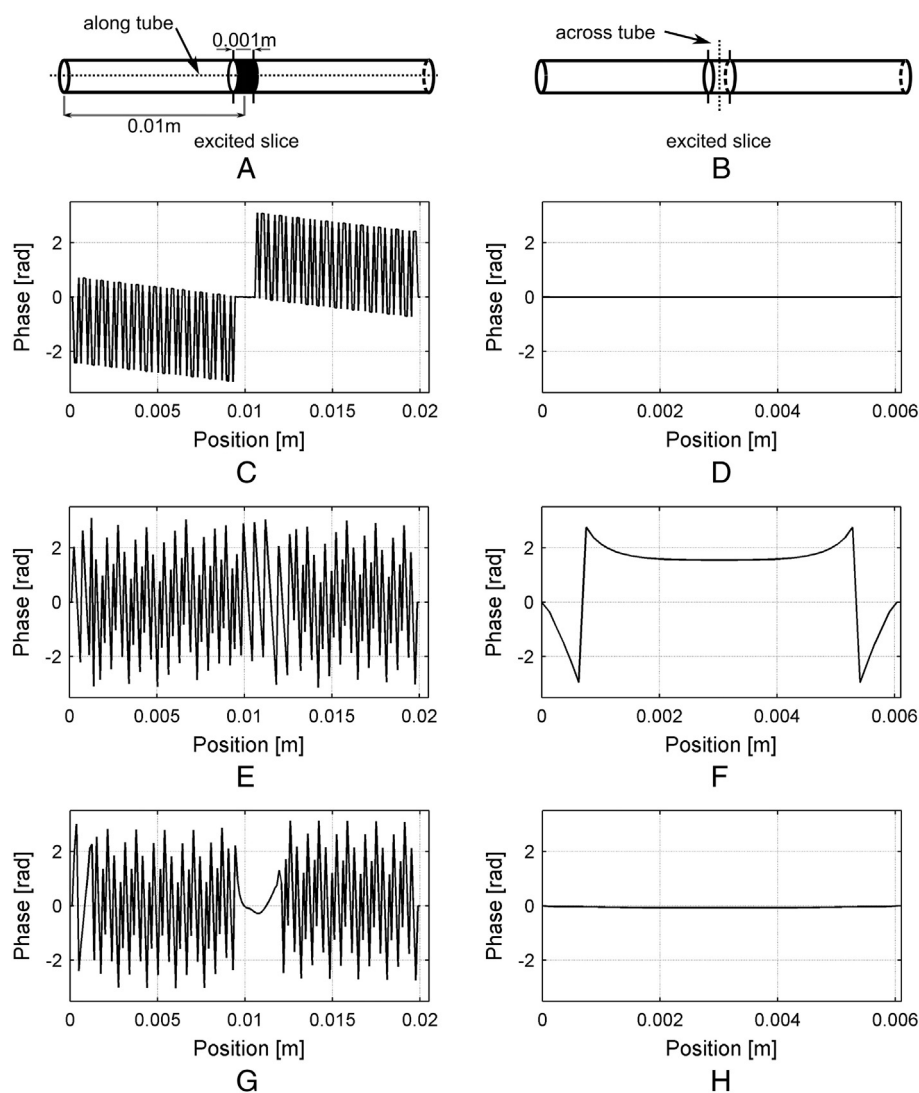


Fig. 6. Curves of transverse magnetization phase of cubic elements just after RF excitation pulse of sinc shape with different conditions, along the tube (along flow direction) or across the tube (perpendicular to flow direction). Dotted lines in sketches (A) and (B) show the direction and location of the cubic elements whose phase is presented. Conditions for curves: (C) without flow, along tube; (D) without flow, across tube; (E) with flow, along tube; (F) with flow, across tube; (G) with flow, along tube + flow compensation gradient; (H) with flow, across tube + flow compensation gradient.

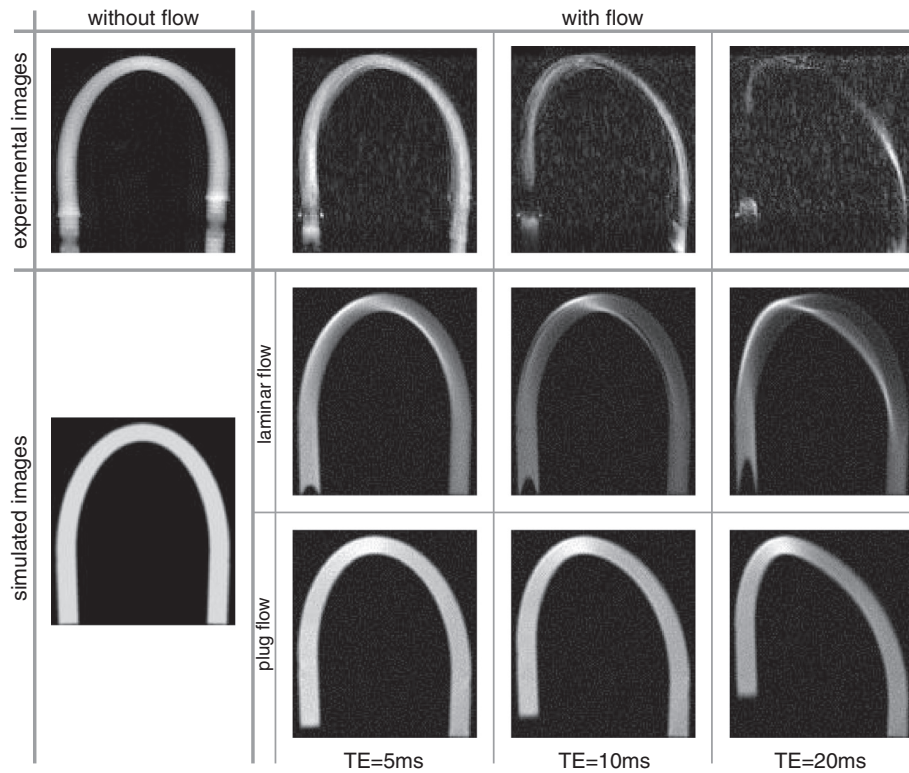


Fig. 7. Comparison of experimental and simulated MR images of the U-bend tube geometry. First- and second-row images (experimental and simulated) were acquired with laminar flow with velocity of 0.38 ms^{-1} . Moreover, to show difference in displacement effect for various flow patterns, the last row contains simulated images with plug flow with velocity of 0.76 ms^{-1} . Frequency encoding in the vertical direction; phase encoding in the horizontal direction.

entrance of the tube, contrarily to experiments. This can be ascribed to the spatially uniform gradients and RF pulses in the computer-simulated sequence. In contrast, in the case of the U-bend geometry, both the simulated and experimental images (Fig. 7) show such an inflow artifact. Here, the slice thickness was three times bigger, and consequently, the spatial nonuniformities in the plane of image could less influence on the image intensity.

In experimental images of the U-bend geometry, at the beginning of the left bend (just after the parabolic signal void), a signal loss appears. In this place, two tubes are connected leading to irregular geometry shapes that are not modeled in the virtual object. These irregular geometries could cause complex flow patterns, like turbulences, and consequently, phase dispersion and image signal loss are induced. Second, higher noise in U-bend experimental

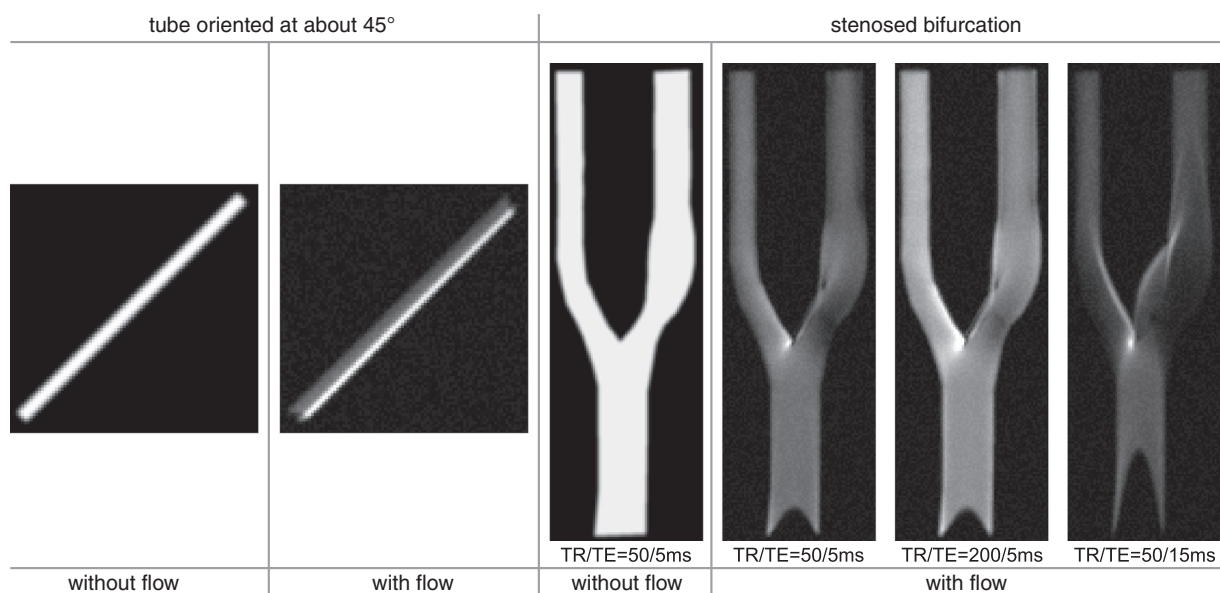


Fig. 8. MR simulated images of the 2D geometries that are commonly tested in other computational solutions of MR flow imaging: (a) straight tube lying diagonal to the gradient axes, frequency encoding in the horizontal direction, phase encoding in the vertical direction; (b) single stenosed carotid bifurcation with stationary flow, frequency encoding in the vertical direction, phase encoding in the horizontal direction.

Table 1

Time measurements of the whole simulation process required to obtain the presented images: flow map generation time (flow simulation) and MRI simulation time.

	Straight tube phantom (sagittal plane)		U-bend phantom		Diagonal tube	Stenosed bifurcation
Dimension	2D	3D	2D	3D	2D	2D
Flow grid size	231 × 498	231 × 498 × 55	577 × 663	577 × 663 × 34	437 × 437	353 × 1105
Object size ^a	320 × 640	320 × 640 × 55	640 × 1280	640 × 1280 × 34	640 × 640	640 × 1280
Image size ^b	64 × 128	64 × 128	128 × 256	128 × 256	128 × 128	128 × 256
Flow simulation time	03 m 28 s	50 m 43 s	29 m 45 s	2 h 30 m 52 s	1 m 01 s	1 h 47 m 15 s
MRI simulation time	12 m 06 s	5 h 58 m 05 s	1 h 08 m 42 s	6 h 14 m 34 s	9 m 53 s	1 h 20 m 07 s

The size of the simulated MR images (in Fig. 7 and 8) can slightly differ from the image size presented in the table due to additional background cubic elements added to objects in order to obtain power of two image sizes. Consequently, the FFT algorithm [40] could be used. After a reconstruction phase, the additional background black areas were cropped from the images.

^a Number of cubic elements.

^b Number of image voxels.

images suggests that there are some additional factors not included in the computational model, e.g., nonuniformities of a transmitter coil and their correlation with flow.

There have been proposed several other approaches in the modeling of MR flow imaging. Some of them can be classified as the Lagrangian-based solutions (e.g., [12,15,19,20]) and the others (e.g., [4,13,16]) as the Eulerian-based ones. In Lagrangian-based solutions, the flow pathlines are calculated first. Then, the temporal tracking of spin magnetizations along these path lines is performed. Such an approach seems to be physically intuitive, but it is known to be computationally expensive and less successful in regions of high flow velocity gradients (e.g., curved geometries) or of complex flow, where artificial sparse filling or lack of spins may be present. In contrast, the most advanced previous Eulerian-based models [4,16] use the Bloch integration with an additional magnetization transport term in 2D objects. The obtained phase and magnitude of magnetization in the center of the echo are directly translated to image intensities. In contrast, in MRI equipment, magnetic signal is acquired during the sampling period and then translated by FFT to an image. Such a computational approach is able to speed up calculations, but it can also lead to difficulties in further model development, e.g., in spiral or radial imaging. To take into account the spatial displacement effect, additional computational mechanisms had to be developed, e.g., mesh transformation [4]. Also, noisy measurements or magnetic field inhomogeneities and susceptibility effects are hard to incorporate.

The proposed approach differs from the existing solutions both at the level of fluid dynamics and MRI simulations. LBM is used in the preprocessing fluid dynamics phase of MR flow imaging for the first time. In this method, the way of object shape definition and geometry discretization as well as boundary condition setting is much more straightforward than in numerical Navier–Stokes equation solvers used in the most sophisticated alternative models [4,19]. Moreover, it is characterized by relatively low computational load (Table 1) and easy accommodation to complex geometries. In previous works on MRI and flow, studies combining LBM with experimental MRI [45,46] can be found. However, in these studies, the process of MRI is not modeled at all, and LBM is used to simulate velocity fields that are then compared with MR velocity measurements.

As far as MRI modeling is concerned, the novelty of our solution is the method of magnetization transport modeling (2D/3D analytical algorithms) and its coupling with the MRI algorithm. The Eulerian coordinate approach is retained, and at the same time, MRI is performed by the discrete-event Bloch equation resolution. Such an approach closely follows the physical process of MRI and, in combination with the magnetization transport algorithm, naturally incorporates flow artifacts. No mechanism such as mesh transformation [4] or compensation of regions of low particle density [19] is needed. This implies that any imaging sequence changes (e.g., additional gradients, RF pulses, different *k*-space trajectories or view

ordering) only require modifications of MRI modeling and no changes in the connection between flow and imaging processes. For instance, a new gradient arrangement in time can be done by required (physically based) changes of *G* value in Eq. (10). As a consequence, the model can be easily adapted, in future studies, in spiral imaging or in b-SSFP sequences to extend existing solutions [7,8] by allowing them to simulate the whole imaging sequence in different geometries with various flows.

The fluid magnetization response to slice-selective RF pulse of different shapes was also incorporated in our solution. A few models (e.g., [8,11,17]) including the flow influence on spin magnetization during slice selection were proposed so far. These models allowed thorough investigation into flow influence on the slice selection step. However, they considered flow modeling only in one direction in simple geometries [11] and did not take into account the whole MRI sequence [8,17] (e.g., without repetitive imaging cycles and space encoding gradients).

There is also no restriction to incorporate other types of flow (e.g., turbulent or pulsatile) in our model since the whole history of magnetization evaluation can be tracked and any changes or even replacements of flow maps during imaging do not require any algorithm changes. Then, comparison with alternative solutions with pulsatile or turbulent flows will be available. However, it is the subject of outgoing research.

On the other hand, our future plans include further development of the model towards our long-term research on complex vascular networks modeling [2,47,48]. In these studies during the last decade, we developed a two-level physiological model of vascularization. It consists of a macroscopic part able to simulate growth and pathological modifications of vascular networks, and a microvascular one responsible for blood flow and contrast agent transport through capillary walls. The usual simulated vascular network consists of thousands of vessel segments in which flow simulations were previously performed using Poiseuille's equation (like in idealized cylindrical tubes). Preliminary tests showed that the solution proposed in this article will be able to simulate more accurate (physically based) flow dynamics in hundreds of vessels and then MRI in a few days at a desktop personal computer. Since we wanted to deal with even more complex vascular structures, high-performance parallel vascular growth algorithms were introduced [49]. Similarly, we have already started to apply parallel computing in modeling of MR flow imaging.

In conclusion, a new approach in computational modeling of MR flow imaging is proposed. The approach couples the flow computation by LBM, MRI simulation by following discrete local magnetizations in time and a new magnetization transport algorithm together. As a result, a fully analytical, flexible and easily extensible solution is created. The validation of our model confirmed that simulated flow images compare well with experimental ones. Moreover, the time of computation has been shown

to be acceptable, even for 3D geometries. However, our future plans to take into account complex vascular structures (dozens and more successive vessels) demand the application of high-performance parallel computing mechanisms.

Acknowledgments

This work was supported in part by Polonium 2012–2013 (French–Polish cooperation program) under the project “MRI analysis and modeling for tissue characterization”, in part by Białystok University of Technology under Grant WI/3/2011 and S/WI/2/2013 and in part by the European Union from the European Social Fund under the “Scholarships for PhD students as a key of developing region Podlasie”.

References

- [1] Meaney JFM, Sheehan J, Boos M. MR Angiography. In: Reimer P, Parizel PM, Meaney JFM, Stichnoth FA, editors. *Clinical MR imaging*. 3rd ed. Berlin: Springer; 2010. p. 549–86.
- [2] Mescam M, Kretowski M, Bezy-Wendling J. Multiscale model of liver DCE-MRI towards a better understanding of tumor complexity. *IEEE Trans Med Imaging* 2010;29(3):699–707.
- [3] Nederkoorn PJ, van der Graaf Y, Eikelboom BC, van der Lugt A, Bartels LW, Mali WP. Time-of-flight MR angiography of carotid artery stenosis: does a flow void represent severe stenosis? *AJNR Am J Neuroradiol* 2002;23:1779–84.
- [4] Lorthois S, Stroud-Rossman J, Berger S, Jou LD, Saloner D. Numerical simulation of magnetic resonance angiographies of an anatomically realistic stenotic carotid bifurcation. *Ann Biomed Eng* 2005;33(3):270–83.
- [5] Nishimura DG, Macovski A, Pauly JM. Magnetic resonance angiography. *IEEE Trans Med Imaging* 1986;MI-5(3):140–51.
- [6] Nishimura DG, Jackson JL, Pauly JM. On the nature and reduction of the displacement artifact in flow images. *Magn Reson Med* 1991;22(2):481–92.
- [7] Gatehouse PD, Firmin DN. Flow distortion and signal loss in spiral imaging. *Magn Reson Med* 1999;41:1023–31.
- [8] Lagerstrand KM, Plewes DB, Vihoff-Baaz B, Forsell-Aronsson E. Flow-induced disturbances in balanced steady-state free precession images: means to reduce or exploit them. *Magn Reson Med* 2009;61:893–8.
- [9] Dyverfeldt P, Gardhagen R, Sigfridsson A, Karlsson M, Ebberts T. On MRI turbulence quantification. *Magn Reson Imaging* 2009;27(7):913–22.
- [10] Zeigler BP, Praehofer H, Kim TG. *Theory of modeling and simulation*. New York: Academic Press; 2000.
- [11] Yuan C, Gullberg G, Parker D. The solution of Bloch equations for flowing spins during a selective pulse using a finite difference method. *Med Phys* 1987;14:914–21.
- [12] van Tyen R, Saloner D, Jou LD, Berger S. MR imaging of flow through tortuous vessels: a numerical simulation. *Magn Reson Med* 1994;31(2):184–95.
- [13] Jou L-D, van Tyen R, Berger SA, Saloner D. Calculation of the magnetization distribution for fluid flow in curved vessels. *Magn Reson Med* 1996;35:577–84.
- [14] Shkarin P, Spencer RGS. Time domain simulation of Fourier imaging by summation of isochromats. *Int J Imaging Syst Technol* 1997;8(5):419–26.
- [15] Siegel JM, Oshinski JN, Pettigrew RI, Ku DN. Computational simulation of turbulent signal loss in 2D time-of-flight magnetic resonance angiograms. *Magn Reson Med* 1997;37:609–14.
- [16] Jou LD, Saloner D. A numerical study of magnetic resonance images of pulsatile flow in a two dimensional carotid bifurcation: a numerical study of MR images. *Med Eng Phys* 1998;20(9):643–52.
- [17] Lewis DP, Tsui BMW, Moran PR. Velocity sensitivity of slice-selective excitation. *Magn Reson Imaging* 1998;16(8):907–16.
- [18] Marshall I. Simulation of in-plane flow imaging. *Concepts Magn Reson* 1999;11:379–92.
- [19] Marshall I. Computational simulations and experimental studies of 3D phase-contrast imaging of fluid flow in carotid bifurcation geometries. *J Magn Reson Imaging* 2010;31(4):928–34.
- [20] Petersson S, Dyverfeldt P, Gardhagen R, Karlsson M, Ebberts T. Simulation of phase contrast MRI of turbulent flow. *Magn Reson Med* 2010;64(4):1039–46.
- [21] Succi S. *The lattice Boltzmann equation for fluid dynamics and beyond*. Oxford: Clarendon Press; 2001.
- [22] Tritton DJ. *Physical fluid dynamics*. Oxford: Oxford University Press; 1988.
- [23] Bloch F. Nuclear induction. *Phys Rev* 1946;70:460–74.
- [24] Bittoun J, Taquin J, Sauzade M. A computer algorithm for the simulation of any nuclear magnetic resonance (NMR) imaging method. *Magn Reson Imaging* 1984;2:113–20.
- [25] Jurczuk K, Kretowski M, Eliat PA, Bellanger JJ, Saint-Jalmes H, Bezy-Wendling J. A new approach in combined modeling of MRI and blood flow: a preliminary study. *Proceedings of the IEEE International Symposium on Biomedical Imaging (ISBI)*, Barcelona; 2012. p. 812–5.
- [26] Temam R. *Navier–Stokes equations: theory and numerical analysis*. Providence, RI: American Mathematical Society; 2000.
- [27] He X, Luo L-S. Lattice Boltzmann model for the incompressible Navier–Stokes equation. *J Stat Phys* 1997;88:927–44.
- [28] Reider MB, Sterling JD. Accuracy of discrete-velocity BGK models for the simulation of the incompressible Navier–Stokes equations. *Comput Fluids* 1995;24(4):459–67.
- [29] Junk M, Klar A, Luo L-S. Asymptotic analysis of the lattice Boltzmann equation. *J Comput Phys* 2005;210:676–704.
- [30] Steinhauser MO. *Computational multiscale modeling of fluids and solids: theory and applications*. New York: Springer-Verlag; 2008.
- [31] Mohamad AA. *Lattice Boltzmann method: fundamentals and engineering applications with computer codes*. New York: Springer-Verlag; 2011.
- [32] Feichtinger Ch, Habich J, Kostler H, Hager G, Rude U, Wellein G. A flexible patch-based lattice Boltzmann parallelization approach for heterogeneous GPU–CPU clusters. *Parallel Computing* 2011;37(9):536–49.
- [33] Bhatnager P, Gross EP, Krook MK. A model for collision processes in gases. I. Small amplitude processes in charged and neutral one-component systems. *Phys Rev* 1954;94(3):511–25.
- [34] Wolf-Gladrow DA. *Lattice-gas cellular automata and lattice Boltzmann models: an introduction*. Berlin-Heidelberg: Springer-Verlag; 2000.
- [35] Fung YC. *Biomechanics: motion, flow, stress and growth*. New York: Springer; 1990.
- [36] Guo Z, Zheng C, Shi B. An extrapolation method for boundary conditions in lattice Boltzmann method. *Phys Fluids* 2002;14(6):2007–10.
- [37] Benoit-Cattin H, Collewet G, Belaroussi B, Saint-Jalmes H, Odet C. The SIMRI project: a versatile and interactive MRI simulator. *J Magn Reson* 2005;173:97–115.
- [38] Jochimsen TH, Schafer A, Bammer R, Moseley ME. Efficient simulation of magnetic resonance imaging with Bloch–Torrey equations using intra-voxel magnetization gradients. *J Magn Reson* 2006;180:29–38.
- [39] Kuperman V. *Magnetic resonance imaging – physical principles and applications*. San Diego: Academic Press; 2000.
- [40] Aibinu AM, Salami MJE, Shafie AA, Najeeb AR. MRI reconstruction using discrete Fourier transform: a tutorial. *World Academy of Science Engineering and Technology*; 2008. p. 179–85.
- [41] Courant R, Friedrichs K, Lewy H. On the partial difference equations of mathematical physics. *IBM J Res Dev* 1967;11:215–34.
- [42] Bernstein MA, King KF, Joe Zhou X. *Handbook of MRI pulse sequences*. Burlington, MA: Elsevier Academic Press; 2004.
- [43] Edelstein WA, Glover GH, Hardy C, Redington JRW. The intrinsic signal to noise ratio in NMR imaging. *Magn Reson Imaging* 1986;3:604–18.
- [44] Krynicki K. Proton spin-lattice relaxation in pure water between 0 °C and 100 °C. *Physica* 1966;32(1):167–78.
- [45] Mantle MD, Bijeljic B, Sederman AJ, Gladden LF. MRI velocimetry and lattice-Boltzmann simulations of viscous flow of a Newtonian liquid through a dual porosity fibre array. *Magn Reson Imaging* 2001;19(3–4):527–9.
- [46] Zeiser T. Combination of detailed CFD simulations using the lattice Boltzmann method and experimental measurements using the NMR/MRI technique. In: Krause E, Jager W, Resch M, editors. *High performance computing in science and engineering*. Berlin Heidelberg: Springer; 2005. p. 277–92.
- [47] Kretowski M, Rolland Y, Bezy-Wendling J, Coatrieux J-L. Physiologically based modeling for medical image analysis: application to 3D vascular networks and CT scan angiography. *IEEE Trans Med Imaging* 2003;22(2):248–57.
- [48] Kretowski M, Bezy-Wendling J, Coupe P. Simulation of biphasic CT findings in hepatic cellular carcinoma by a two-level physiological model. *IEEE Trans Biomed Eng* 2007;54(3):538–42.
- [49] Jurczuk K, Kretowski M, Bezy-Wendling J. Vascular system modeling in parallel environment – distributed and shared memory approaches. *IEEE Trans Inf Technol Biomed* 2011;15(4):668–72.